

PRODUCTION AND DECAY OF Z BOSONS AT THE SLC*

G. J. Feldman

Stanford Linear Accelerator Center
Stanford University, Stanford, California 94309, USA

INTRODUCTION

My lectures at Cargèse covered the very first physics results from the SLAC Linear Collider (SLC). At the time of this writing (December 1989), it seems most sensible to present a review of the results that were presented at the school in an updated form. The organization of this report will be to give a brief introduction to linear colliders and the SLC, then to describe the MARK II detector, and finally to review the current status of the three major physics topics discussed at Cargèse:

1. the Z line shape, from which we deduce the Z mass and width, and the number of neutrino species,
2. the partonic structure of hadronic decays and a measurement of α_s , and
3. searches for new quarks and leptons.

LINEAR COLLIDERS AND THE SLC

The SLC is the first operating single-pass e^+e^- collider. We built it for two reasons:

1. to develop the technology which will be used for all future e^+e^- colliders with energies higher than 200 GeV, and
2. to make the first study at the Z mass.

Both reasons were essential, but the former will provide the lasting contribution of the SLC.

Why will linear colliders rather than storage rings provide the technology needed to explore higher energies in e^+e^- annihilation? Burton Richter studied the scaling laws for storage rings in 1976.¹ There are two factors in the cost of a high-energy storage ring. Most of the costs scale as the size of the ring—tunnels, magnets, vacuum systems, etc. The one cost that does not scale with the size of the ring is the RF system, which is required to make up the energy lost to synchrotron radiation. The voltage required to restore the lost energy is proportional to the fourth power of the energy and

* Work supported by Department of Energy contract DE-AC03-76SF00515.

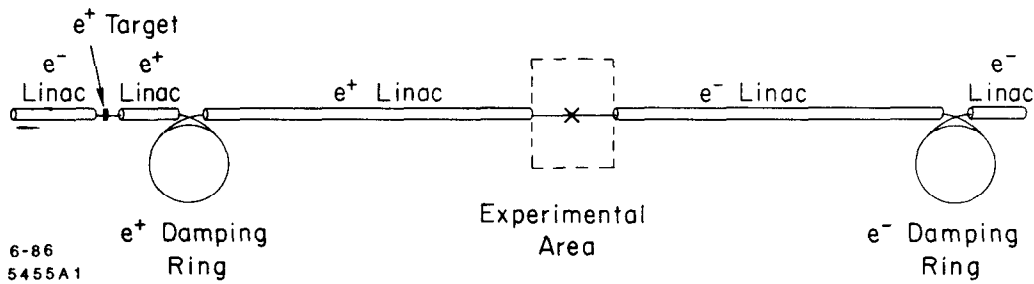


Fig. 1. Schematic of a generic linear collider.

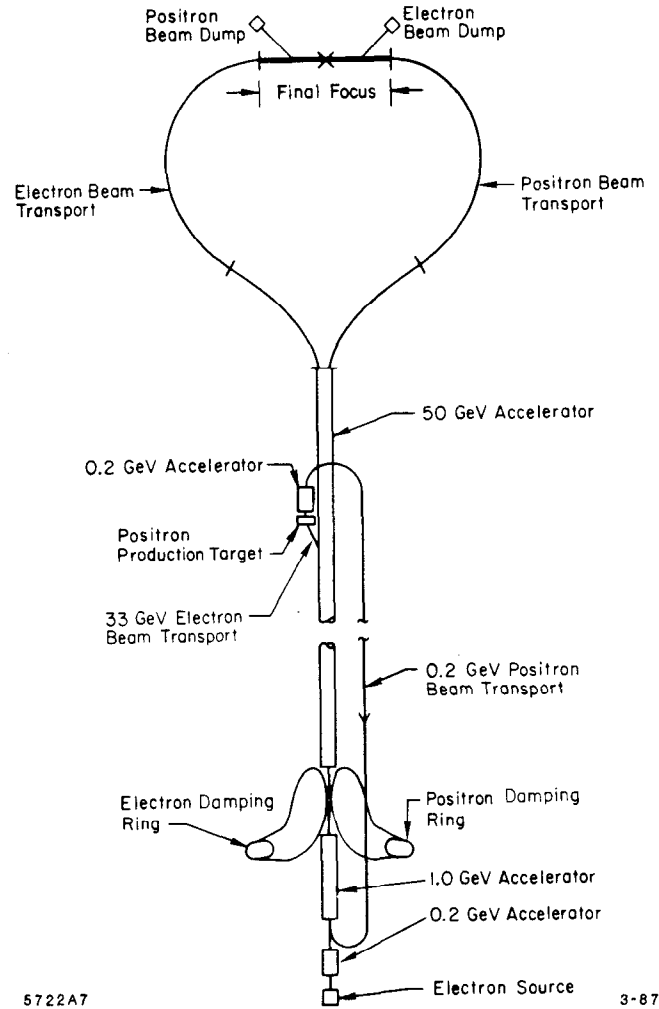


Fig. 2. Schematic of the SLC.

inversely proportional to the radius of curvature. Thus, simplifying Richter's argument considerably, we can write

$$C = \alpha R + \beta \frac{E^4}{R} \quad (1)$$

where C is the cost, R is the radius, E is the energy, and α and β are constants. Optimizing the cost by setting the derivative of Eq. (1) with respect to R to zero yields the result that both the cost and size of a storage ring scale with E^2 .

We can thus estimate the cost of a 1 TeV storage ring by assuming that LEP II is an optimized 200 GeV storage ring and using this scaling law. The result is that such

a ring would be 675 km in circumference and cost 17.5 billion dollars. Even by our new sense of reasonableness set by the SSC scale, this seems unreasonable and suggests that we should pursue an alternate technology. Both the cost and size of a linear collider, of course, scale with energy, making it appear to be a more promising approach.

Figure 1 shows a generic linear collider. It has three main accelerators: an electron linac to produce positrons, and positron and electron linacs to accelerate the beams to high energy. It also has two damping rings to reduce the emittance of the beams.

Figure 2 shows the only present example of a linear collider, the SLC. Please note that this design is topologically equivalent to the generic linear collider with the present SLAC linac serving as all three required linacs. A positron return line and two arcs have been added to transport the particles to the required locations; in principle, these transport lines do not affect the basic functioning of the collider.

The SLC was originally scheduled to begin taking physics data in January 1987. However, since it represented a new and difficult technology, we obtained the first reasonable luminosity in late March 1989, and observed the first Z boson decay on April 11, 1989. Since that time, we have collected 19 nb^{-1} of integrated luminosity and have observed about 500 Z decays.

THE MARK II DETECTOR

The MARK II detector began life as the second general purpose detector at the 7 GeV storage ring SPEAR. Later it was moved to the 29 GeV storage ring PEP. After it was selected to be the first SLC detector, it was upgraded, tested at PEP, and finally moved to the SLC. The MARK II Collaboration presently consists of approximately 130 physicists from nine institutions.²

A drawing of the MARK II detector³ is shown in Fig. 3. The principal components that we will be interested in here will be the drift chamber, the calorimeters, and the luminosity monitors.

The drift chamber is a 72-layer, minijet cell, cylindrical chamber⁴ immersed in 4.75 kG solenoidal magnetic field. It tracks charged particles in the region $|\cos \theta| < 0.92$, but the efficiency and momentum resolution begin to deteriorate at $|\cos \theta| = 0.82$. Without a vertex constraint, the momentum resolution is about 0.5% p (p in GeV/c).

There are two sets of electromagnetic calorimeters, which, together, detect photons in the region $|\cos \theta| < 0.96$. The central calorimeters are lead-liquid argon sandwich ionization chambers⁵ with an energy resolution of about $14\%/\sqrt{E}$ (E in GeV). The forward and backward calorimeters are composed of lead-gas proportional tube sandwiches with energy resolution of about $22\%/\sqrt{E}$. Both calorimeters have a strip geometry with three or four strip directions for stereographic reconstruction.

Figure 4 shows a close-up of the region around the beam-line. Note the two luminosity monitors at small angles, the Small Angle Monitor (SAM), followed at smaller angles by the MiniSAM.

A typical hadronic Z decay is shown in Fig. 5(a). The two jet structure, shown graphically in the Lego plot of Fig. 5(b), and the charged multiplicity of about 20 tracks are typical of these events. About 7/8 of visible Z decays are into hadronic modes. The remainder are split among e , μ , and τ pairs. A τ pair decay is shown in Fig. 6, in which one of the τ 's decays into a 16 GeV/c muon and the other decays into a 17 GeV/c electron.

MARK II AT SLC

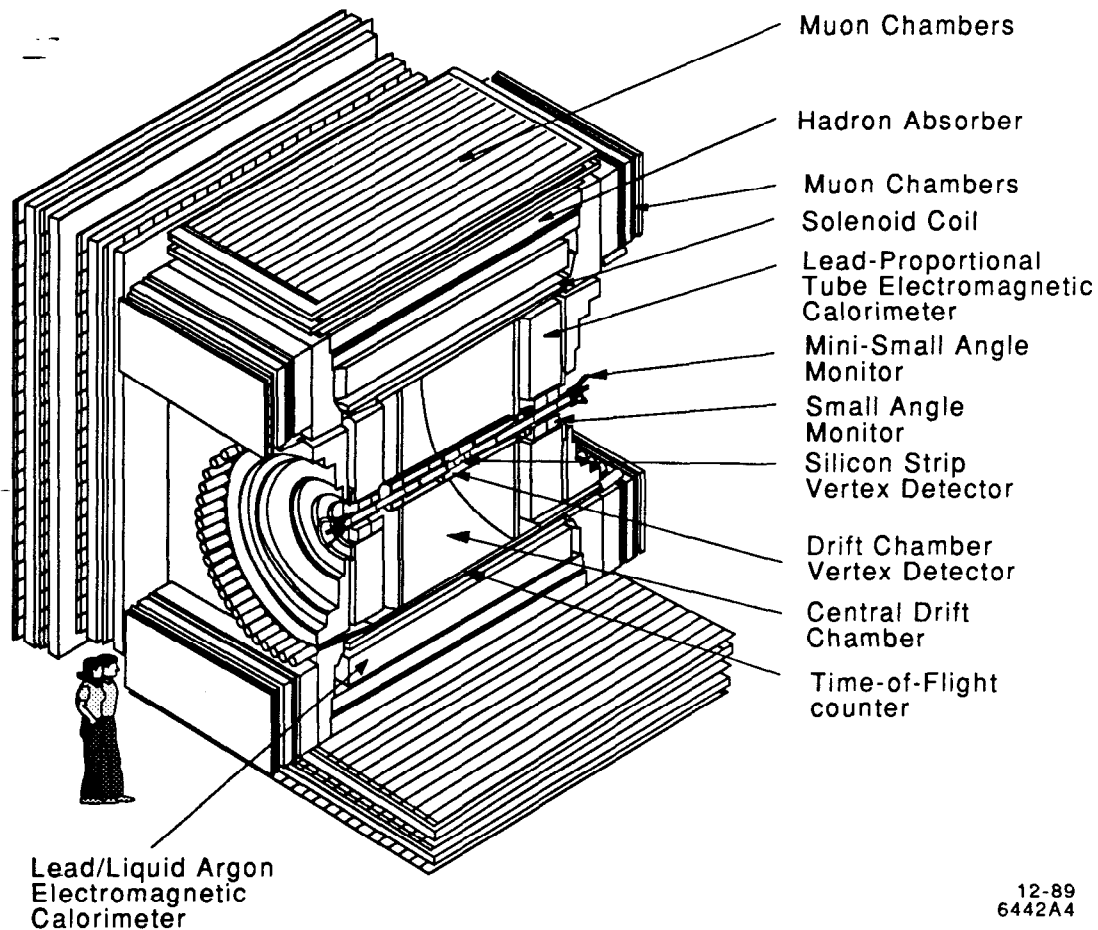


Fig. 3. The MARK II detector.

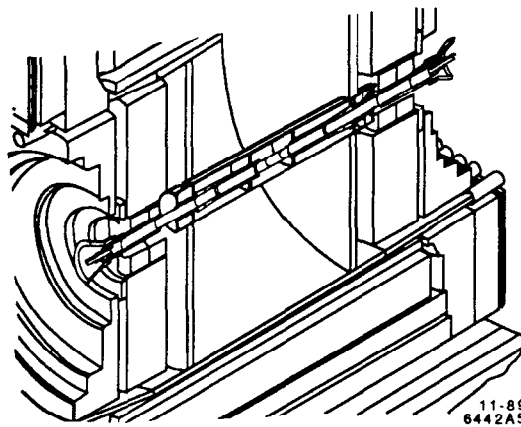


Fig. 4. Detail around the beam line of the MARK II detector.

The six main MARK II triggers are listed in Table 1. Monte Carlo simulations indicate that the charged and neutral triggers are 97% and 95% efficient for Z hadronic decays, respectively. In addition to being highly redundant, they are complementary in that the charged trigger is more efficient in the central region, while the neutral trigger is more efficient in the forward and backward regions. Together, they are calculated to be 99.8% efficient.

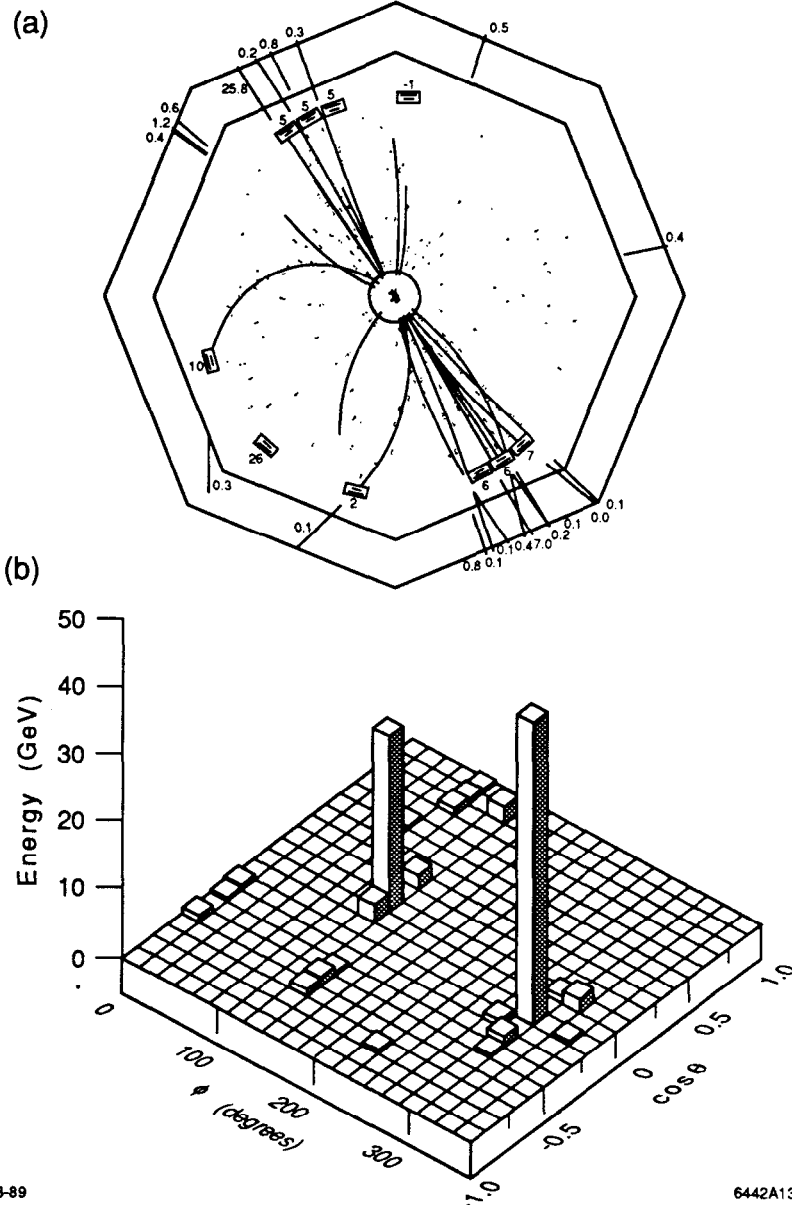


Fig. 5. (a) A computer reconstruction of a typical hadronic Z decay viewed along the beam axis. (b) A plot of the detected energy for this event as a function of the azimuthal angle and the cosine of the polar angle.

The random trigger is used to correct for beam-induced backgrounds. For example, in all MARK II SLC analyses, randomly triggered events are combined with Monte Carlo simulations of physical processes to give a complete simulation of both the physics and the backgrounds.

Z RESONANCE PARAMETERS⁶

We want to determine the Z boson resonance parameters by comparing the rate of Z formation in e^+e^- annihilation (Fig. 7) as a function of the center-of-mass energy, E , with that for a process with a known cross section, Bhabha (e^+e^-) scattering (Fig. 8). To accomplish this, we have to do four things:

1. measure E ,

spectrometers. The electron beam first passes through a horizontal bend and emits a horizontal swath of synchrotron radiation in the initial electron beam direction. It then passes through an accurately-measured spectrometer magnet which bends it down. Finally, it traverses a second horizontal bend to give another swath of synchrotron radiation in the direction of the outgoing beam. The two swaths of synchrotron radiation are intercepted by a phosphorescent screen. It is clear that the mean energy of beam can be measured from the knowledge of three quantities:

1. the magnetic-field integral of the spectrometer magnet,
2. the distance between the center of the spectrometer magnet and the screen, and
3. the distance between the two synchrotron radiation swaths on the screen.

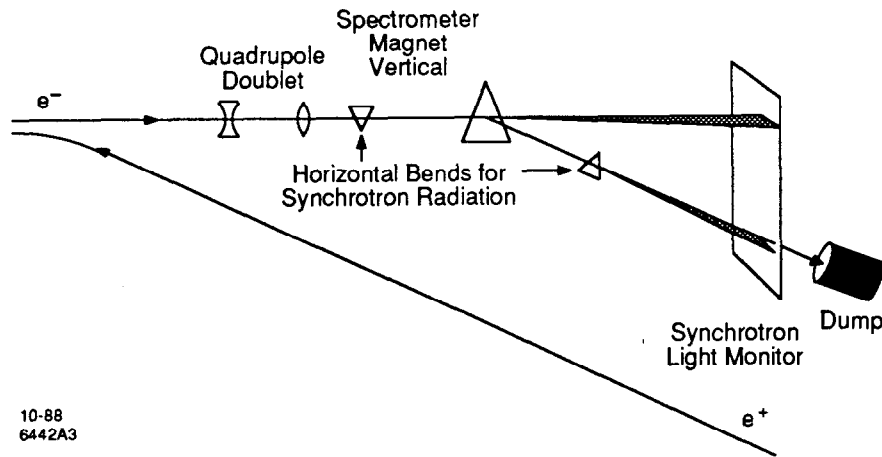


Fig. 9. Schematic of one of the energy spectrometers.

The spectrometer magnet field integral has been calibrated to a few parts in 10^5 by two independent techniques and is constantly measured by a rotating coil. The distance between the magnet center and the screen is determined to high precision by surveying techniques, and the distances on the screen are calibrated by accurately placed fiducial wires.

The systematic uncertainties in the measurement of each beam (itemized in Table 2) total to 20 MeV.

The energy spread of each beam is also measured to about 30% accuracy by the increased dispersion caused by the spectrometer magnet. The mean energy and energy spread are measured on every SLC pulse and are read by the MARK II on every trigger.

Table 2: Systematic uncertainties in the energy measurement of each beam.

Item	Uncertainty (MeV)
Magnetic measurement	5
Detector resolution	10
Magnet rotation	16
Survey	5
Total	20

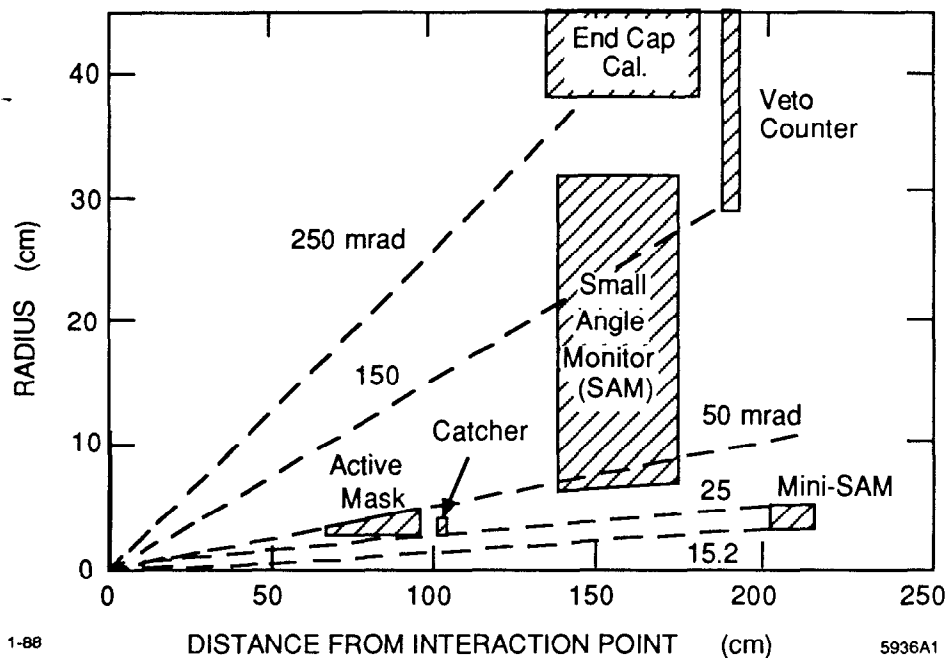


Fig. 10. Geometrical acceptances of the SAM and MiniSAM.

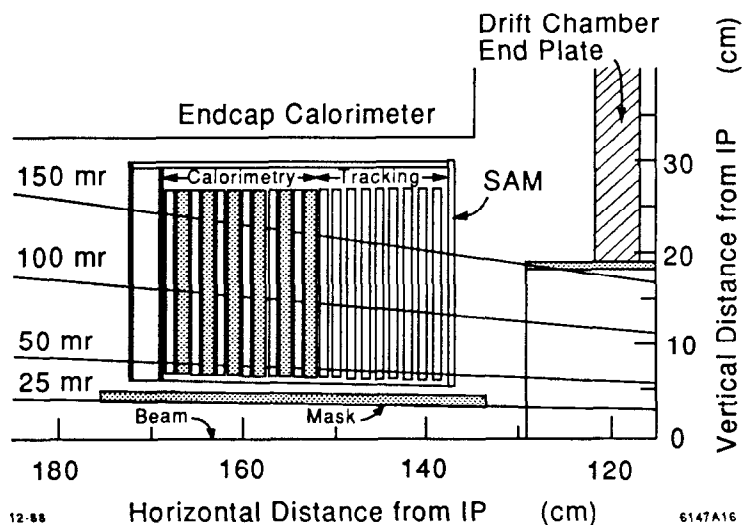


Fig. 11. The Small Angle Monitor (SAM).

Luminosity Measurements

To obtain the optimum absolute and relative luminosity measurements we use a well-defined fiducial region of the SAM to measure the absolute luminosity, while we use the total SAM and the MiniSAM to determine the relative, or point-to-point, luminosity. The geometrical acceptance of these detectors is illustrated in Fig. 10.

A drawing of the SAM is shown in Fig. 11. Each SAM consists of nine layers of drift tubes for tracking and a six-layer lead-proportional-tube sandwich for measuring the electron energy and position. A typical event is shown in Fig. 12. The tracking information is not always available due to backgrounds, but the calorimetric reconstruction of the electron pulse is unmistakable and background free. The angular resolution from the shower reconstruction is about a milliradian.

The technique for determining the absolute luminosity was to count events with both the electron and positron tracks in the angular region $65 < \theta < 160$ mrad with

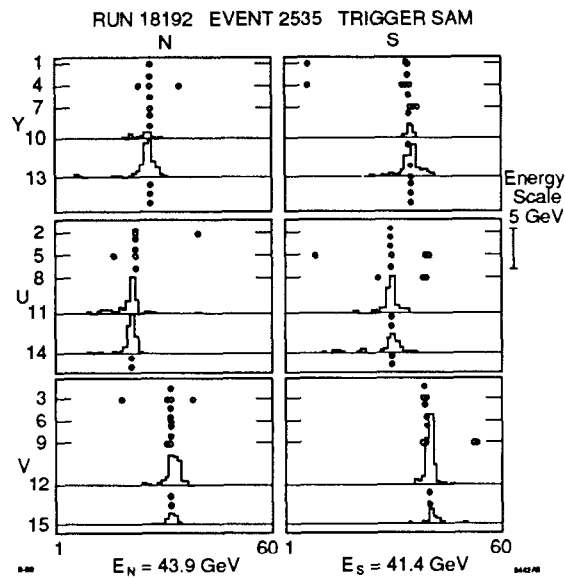


Fig. 12. A typical SAM event.

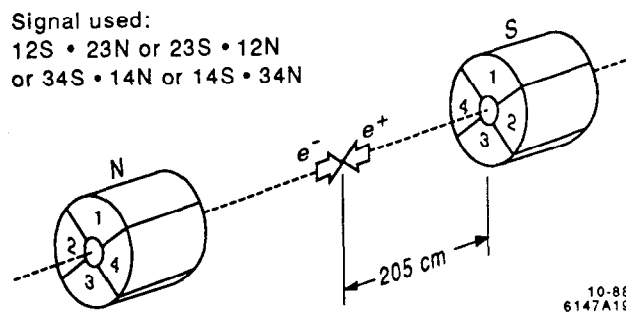


Fig. 13. The MiniSAMs.

unit weight and events with only one track in this with region with half weight. This is a standard technique to reduce the sensitivity of the measurement to possible misalignments and detector resolution.

The cross section corresponding to the precise region was calculated⁸ to be 25.2 nb at 91.1 GeV.

The systematic uncertainties in the absolute luminosity measurement total 3.0% and are equally divided between unknown higher-order radiative corrections and the effect of detector resolution on the SAM precise region acceptance.

The most important part of the point-to-point luminosity measurement are the MiniSAMs, a drawing of which is shown in Fig. 13. These are simple tungsten-scintillator sandwiches divided into four quadrants which are separately read out.

The requirement for detecting a Bhabha scattering event in the MiniSAMs is:

1. a back-to-back pair of adjacent quadrants on each side, each of which has 25 GeV more energy than the other pair of quadrants on that side,
2. time-of-flight measurement in all quadrants with more than 18 GeV consistent with the Bhabha scattering.

The efficiency of the MiniSAMs varies from 91% to > 99%, depending on scan point; and the backgrounds, measured from non-back-to-back quadrants, vary from 0 to 3.5%. We estimate the point-point systematic error to be the larger of 1% or the background subtraction.

Z Decay Event Selection

Z production is the dominant annihilation process, so the selection criteria can be quite loose. The only possible backgrounds come from beam-gas interactions and $\gamma\text{-}\gamma$ interactions. Both of these processes leave a large amount of energy in at most one of the forward-backward hemispheres.

Accordingly, the criteria for hadronic Z decays are:

1. ≥ 3 charged tracks from a cylindrical volume around the interaction point with a radius of 1 cm and a half-length of 3 cm, and
2. at least 0.05 E visible in both the forward and backward hemispheres.

These criteria give an efficiency of $94.5 \pm 0.5\%$.

The only major sources of backgrounds are from beam-gas and two photon interactions. With the above selection criteria, we have determined that both are negligible, much less than one event in the entire data sample.

To increase our statistical precision slightly, we also accept those leptonic Z decays for which the efficiency is high and the identification and interpretation is clear, namely, μ and τ pairs in the angular region $|\cos\theta| < 0.65$. To avoid backgrounds from $\gamma\text{-}\gamma$ interactions, we require a minimum of 0.10 E visible energy for τ pairs. The efficiencies for detecting μ and τ pairs within the fiducial angular region are $99 \pm 1\%$ and $96 \pm 1\%$, respectively.

The data are shown in Fig. 14. Note that we plot an unusual quantity, but one that is closely related to what we actually measure, the cross sections for all hadronic decays and $\mu^+\mu^-$ and $\tau^+\tau^-$ with $|\cos\theta| < 0.65$.

Fits to the Data

We perform maximum-likelihood fits using Poisson statistics to a relativistic Breit-Wigner line shape

$$\sigma(E) = \frac{12\pi}{m^2} \frac{s\Gamma_{ee}(\Gamma - \Gamma_{inv})}{(s - m^2)^2 + s^2\Gamma^2/m^2} [1 + \delta(E)] \quad , \quad (2)$$

where Γ is the total width and Γ_{inv} is the partial width into invisible decay modes, *i.e.*, into neutrinos and neutrino-like particles. Large effects due to initial state radiation, represented in Eq. (2) by $[1 + \delta(E)]$, are calculated by an analytic form due to Cahn.⁹ Alexander *et al.* have shown that this form has more than sufficient accuracy for our purposes.¹⁰

A Breit-Wigner shape has three parameters, a position, a width, and a height. We can fit for these three parameters as m , Γ , and Γ_{inv} , or equivalently, the number of neutrino species, N_ν .

The mass and width clearly determine the position and width of the resonance. The height is most sensitive to the third parameter, Γ_{inv} . This comes about because a Breit-Wigner is proportional to the partial width to the initial state times the partial width to the final state. The partial width to the initial state, e^+e^- , is well determined in the Standard Model. The final state can be taken to be all of the final states that we can see, in principle, in our detector, *i.e.*, all states except those into neutrino pairs (or pairs of neutrino-like objects).

Another way of viewing this is the following: If we could detect all of the final states, and if we integrated the resonance over energy, then we would find that the

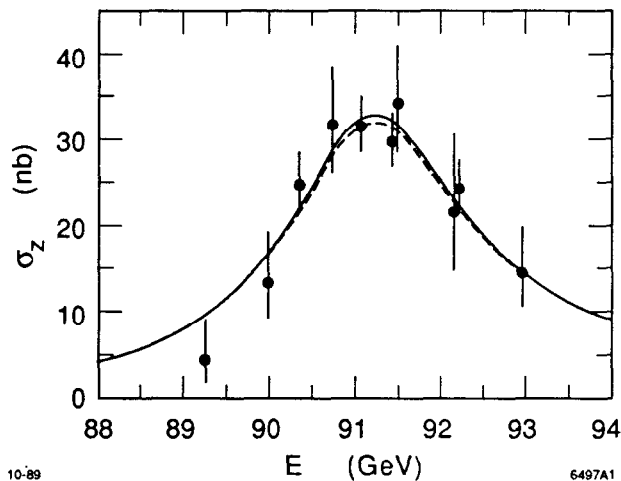


Fig. 14. The cross sections for all hadronic decays and $\mu^+\mu^-$ and $\tau^+\tau^-$ with $|\cos\theta| < 0.65$. The dashed curve represents the result of the Standard Model fit. The solid curve represents the free ν fit and the unconstrained fit, which are indistinguishable.

integral only depends on the width to the initial state. This is a statement that we produce a Z and that it subsequently decays with unit probability. What we do not detect, then, must be those decays into neutrino pairs.

We perform three fits which differ in their reliance on the Standard Model, and thus address different questions that one may wish to ask.

1. In the “Standard Model fit,” m is the only parameter that is varied. The widths are taken to have their Standard Model values corresponding to the decays into five quarks and three charged and neutral leptons.
2. In the “free ν fit,” both m and Γ_{inv} are allowed to vary. The visible width is constrained to its Standard Model value. The rationale for this twofold:
 - (a) New particle production in the quark-lepton sector might be expected to show up first with the lightest of particles, which, from the three examples we have seen so far, are the neutrinos.
 - (b) Visible new particle production would probably show up first in the observation of distinctive decays.
3. Finally, the “unconstrained fit” allows all three parameters to be varied.

These fits are displayed in Fig. 14. The mass values from the three fits are identical at

$$m = 91.14 \pm 0.12 \text{ GeV}/c^2 \quad . \quad (3)$$

All of the systematic errors in the mass determination are small, with the largest source of systematic uncertainty, included in the quoted errors, being 35 MeV for the absolute energy determination.

The total width Γ is only determined by the unconstrained fit. The value of

$$\Gamma = 2.42_{-0.35}^{+0.45} \text{ GeV} \quad (4)$$

is almost exactly the same as the Standard Model value of 2.45 GeV.¹¹ The errors on the width are large because a good measurement of the width requires substantial data at ± 2 GeV from the peak. We did not take very much data that far from the peak

because the rate was just too low with our luminosity. Again all the systematic errors are small compared to the statistical error. The most significant contribution is 50 MeV from the uncertainty in the MiniSAM efficiency and background corrections.

The value

$$N_\nu = 2.8 \pm 0.6 \quad (5)$$

is taken from the free ν fit. This translates into the upper limit

$$N_\nu < 3.9 \text{ at } 95\% \text{ C.L.} \quad (6)$$

which provides strong evidence that the number of light neutrino species is limited to the three that we have already discovered. The quoted errors include a contribution of 0.45 from the uncertainty in the absolute luminosity measurement.

Relationship between the Mass and $\sin^2\theta_W$

The electroweak mixing angle, θ_W , can be expressed in terms of the Z mass by the relation

$$\sin 2\theta_W = \left(\frac{4\pi\alpha}{\sqrt{2}G_F m_Z^2 (1 - \Delta r)} \right)^{1/2} \quad (7)$$

where Δr represents weak radiative corrections. These corrections arise from loops and are sensitive to the masses of high mass particles.

The most common definition of $\sin^2\theta_W$ is the Sirlin form,¹² which is defined as

$$\sin^2\theta_W \equiv 1 - \frac{m_W^2}{m_Z^2} \quad (8)$$

For specific values of the two unknown masses in the Standard Model,

$$m_t = m_H = 100 \text{ GeV}/c^2 \quad (9)$$

our measured m_Z of 91.14 ± 0.12 implies

$$\sin^2\theta_W = 0.2304 \pm 0.0009 \quad (10)$$

The dependence of $\sin^2\theta_W$ on these two masses is shown in Fig. 15.

PARTONIC STRUCTURE OF HADRONIC DECAYS¹³

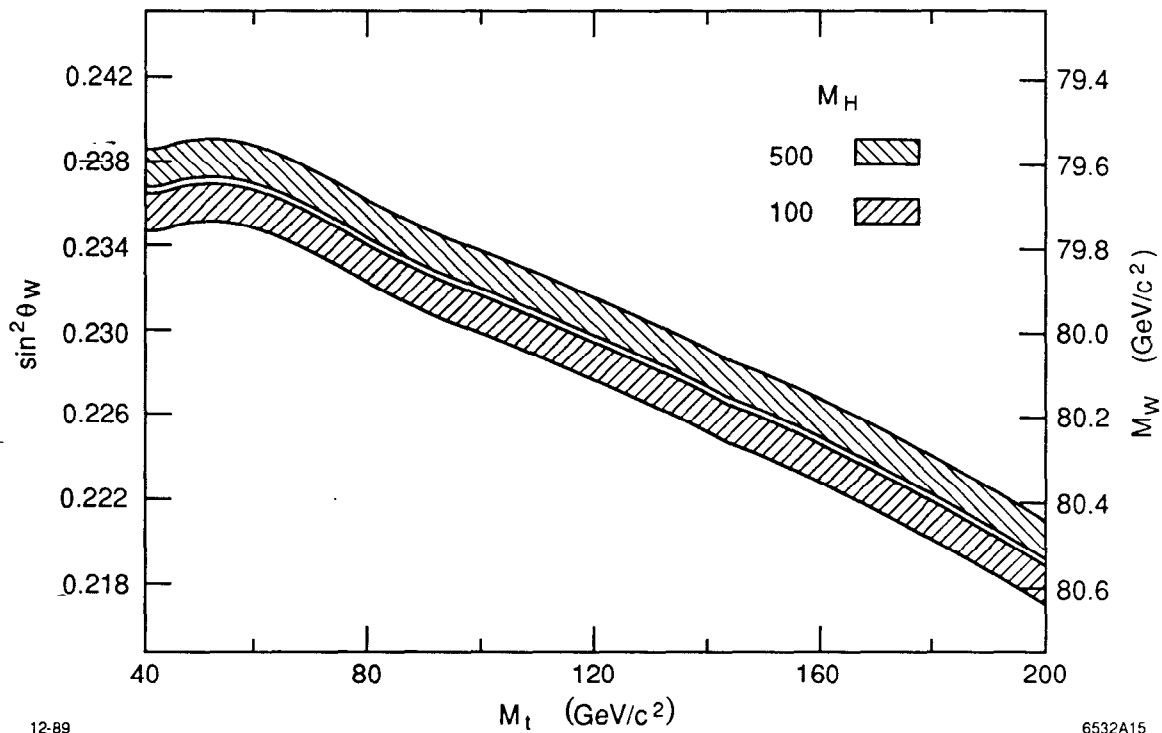
In addition to the underlying quark-antiquark structure of hadronic decays, QCD predicts the existence of multijet events due to gluon bremsstrahlung. By studying event shape parameters and counting jets, we can test the predictions of QCD and look for the existence of other processes.

In order to ensure well-measured momenta and a high tracking efficiency, the event selection is more restrictive for this study than for the Z line shape. Events were required to have at least seven charged tracks in the region $|\cos\theta| < 0.82$ and have at least 0.5 E visible in charged and neutral energy.

Shape Parameters

Figure 16 shows the distribution in thrust, T , which is defined

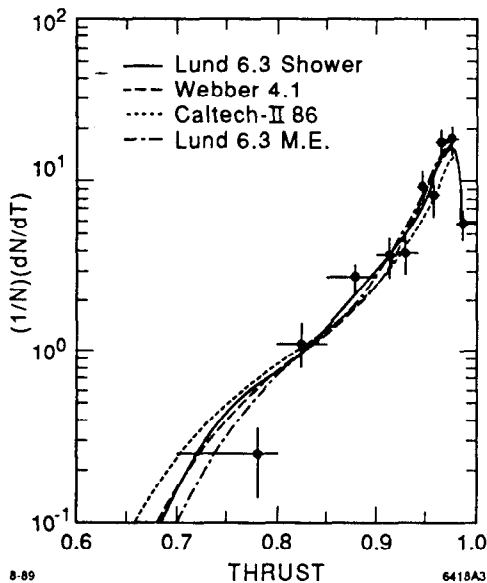
$$T = \left(\frac{\sum_i |p_i \cdot \hat{t}|}{\sum_i |p_i|} \right)_{max} \quad (11)$$



12-89

6532A15

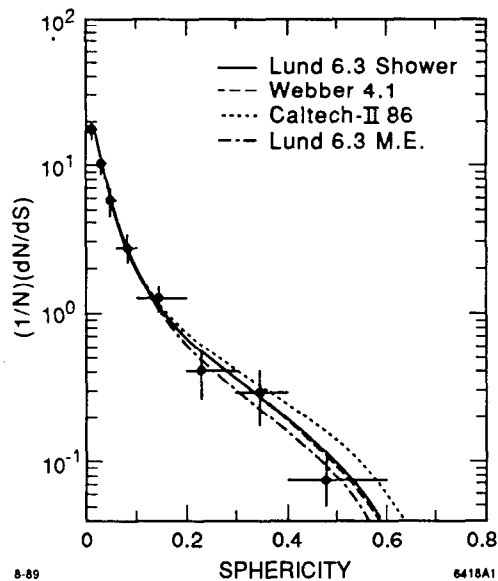
Fig. 15. $\sin^2 \theta_W$ as a function of the mass of the top quark for two values of the Higgs boson mass. The bands represent ± 1 standard deviation about the values derived from Eq. (7).



8-89

6418A3

Fig. 16. Thrust values shown with four Monte Carlo simulations.



8-89

6418A1

Fig. 17. Sphericity values shown with four Monte Carlo simulations.

where \hat{t} is defined as the thrust axis. Thrust is a linear measure of the departure from a two-jet shape. The data are compared with four Monte Carlo simulations: the Lund shower parton model (Lund 6.3 shower),¹⁴ the Webber–Marchesini parton shower model (Webber 4.1),¹⁵ the Gottschalk–Morris parton shower model (Caltech-II 86),¹⁶ and the Lund model based on the second-order QCD matrix element calculated by Gottschalk and Shatz (Lund 6.3 M.E.).¹⁷ In general, the last of these models is not expected to agree well with the data, since it is explicitly incapable of producing more than four jets. For the thrust distribution, all of the models describe the data well.

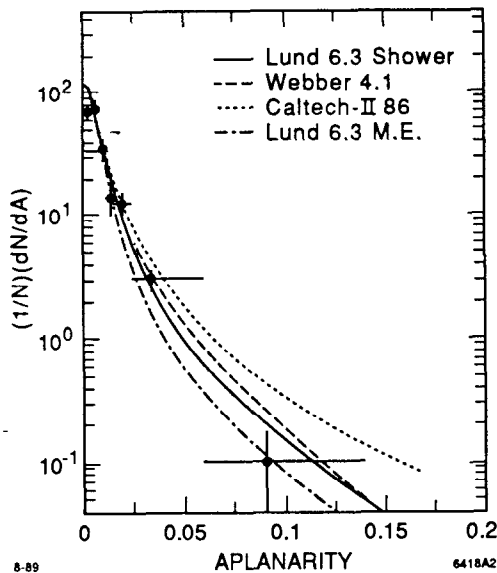


Fig. 18. Aplanarity values shown with four Monte Carlo simulations.

Figure 17 shows the distribution in sphericity, S . This is also a measure of deviation from a two-jet shape, but using p_i^2 rather than p_i . It can be expressed as

$$S = \left(\frac{3 \sum_i p_i^2}{2 \sum_i p_i^2} \right)_{min} \quad (12)$$

Again the models describe the data well.

Figure 18 shows the distribution of aplanarity, A . It is a measure of amount of momentum out of an optimum plane. This is a measure of four or more jets, since conservation of momentum requires three jets to lie in a plane. Aplanarity can be written as

$$A = \left(\frac{3 \sum_i p_{out,i}^2}{2 \sum_i p_i^2} \right)_{min} \quad (13)$$

The parton shower models describe the data well, while the Lund matrix element model underestimates the amount of aplanarity, as expected.

Jet Counting

A cluster algorithm developed by the JADE group is used to count jets.¹⁸ In each event, the quantity $y_{ij} = m_{ij}^2/E_{vis}^2$ is calculated for all pairs of particles i and j . The pair with the smallest invariant mass, m_{ij} is combined to form a pseudoparticle with four-momentum $p_i + p_j$. This procedure is repeated until the smallest y_{ij} exceeds an adjustable threshold value y_{cut} . The hadronic jets defined in this way have the property that they are very similar to partonic jets, as created in a QCD shower simulation.

Figure 19 shows the fraction of events with n jets as a function of y_{cut} . There is good agreement between the data and the Lund parton shower model.

Energy Dependence and Measurement of α_s

Figure 20 shows the mean values of three shape parameters and the fraction of three jet events for $y_{cut} = 0.08$ as a function of center-of-mass energy. The lower energy data come from the MARK II experiment¹⁹ at 29 GeV and other experiments.²⁰⁻²⁷

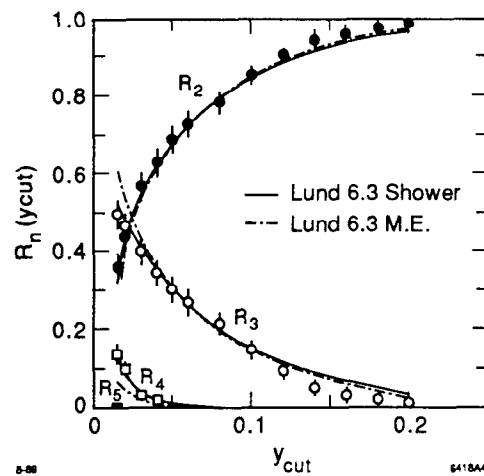


Fig. 19. The observed fraction of events with n jets as a function of y_{cut} . The curves show two Monte Carlo simulations.

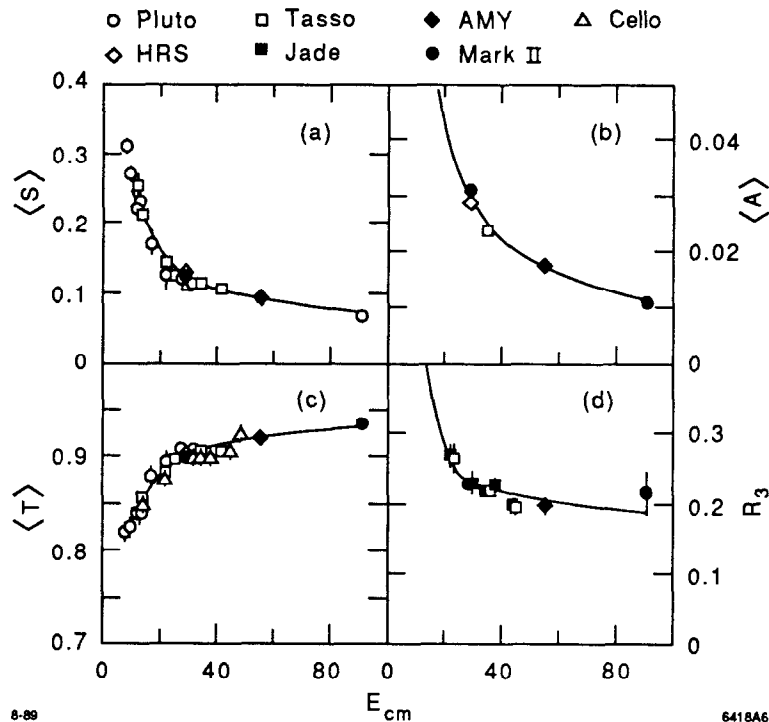


Fig. 20. The mean values of (a) sphericity, (b) aplanarity, (c) thrust, and (d) the three-jet fraction for a y_{cut} of 0.08 versus center-of-mass energy.

The curves show a strong dependence with energy at low energy and a more gradual dependence at high energy. The former is due to fragmentation effects, while the latter is due to the running of the strong coupling constant, α_s .

We have made a determination of α_s at 29 and 91 GeV with the MARK II²⁸ by counting the fraction of three jet events with y_{cut} between 0.04 and 0.14. Using the second-order calculation of Kramer and Lampe,²⁹ with $Q^2 = E^2$ in the \overline{MS} renormalization scheme, we obtain

$$\alpha_s = 0.149 \pm 0.002 \pm 0.007 \text{ at } 29 \text{ GeV} \quad , \quad (14)$$

and

$$\alpha_s = 0.123 \pm 0.009 \pm 0.005 \text{ at } 91 \text{ GeV} \quad , \quad (15)$$

where the first error is statistical and the second systematic. These results, shown in Fig. 21, are consistent with the QCD prediction for the running of α_s .

SEARCHES FOR NEW QUARKS AND LEPTONS³⁰

The great power of e^+e^- annihilation is that all pairs of fundamental particles with masses less than half the center-of-mass energy are copiously produced. We have started our searches for new particles with quarks and leptons, but the techniques are quite general and would have uncovered other types of new particles if they were present in sufficient numbers. Specifically, we have searched for the top quark, a fourth-generation charge $-1/3$ quark (b'), and heavy, unstable, neutral leptons. (We have, of course, also searched for new charged leptons, but due to limited statistics, our limits are not higher than those already obtained at TRISTAN.)

We expect new quarks and leptons to decay through virtual W decay. However, there are several other possibilities that we have explored. A b' quark could decay

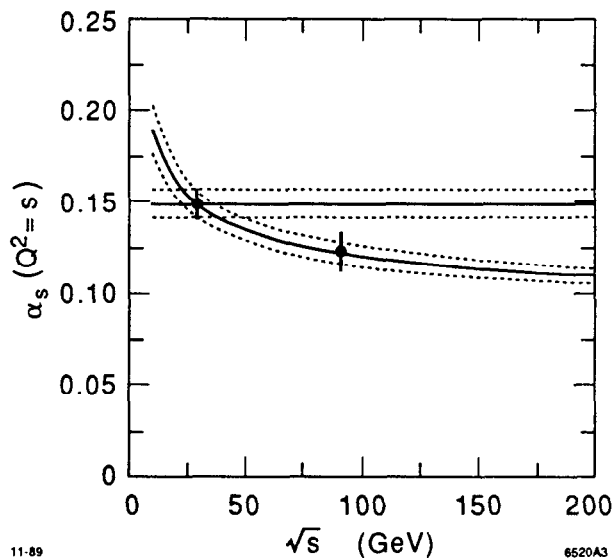


Fig. 21. The values of α_s determined from the three-jet fraction versus center-of-mass energy. The solid lines show a constant value of α_s , and the values expected from QCD normalized to the data at 29 GeV. The dotted lines show the 1σ errors on the values extrapolated from 29 GeV.

through penguin diagrams into $b + \text{gluon}$ or $b + \gamma$ if there is sufficient mixing angle suppression of the charged current decays.³¹ If charged Higgs bosons exist with masses less than those of new quarks or leptons, they, rather than virtual W 's will mediate the decays of these fermions.

We use two complementary techniques to search for new particles: a search for isolated particles and a search for nonplanar events.

For both types of searches, the event selection is intermediate between that for the study of resonance parameters and that for the study of partonic properties. Explicitly, we require events to have at least six charged tracks in the region $|\cos\theta| < 0.85$ and have at least $0.1 E$ visible in charged and neutral energy. In addition, in order to insure that the events are well contained within the detector, the thrust axis of each event be in the region $|\cos\theta| < 0.80$.

In the search for isolated tracks, we define an isolation parameter, ρ , as follows: Excluding the candidate track, we use the jet-finding algorithm, with effectively a low value of y_{cut} , to form a number of jets. We then define

$$\rho \equiv \min_j [(2E(1 - \cos\theta_j))^{1/2}] \quad , \quad (16)$$

where E is the track energy in GeV and θ_j is the angle between the track and each jet axis. We define an isolated track to be one with $\rho > 1.8$.

Figure 22 shows the maximum ρ for each event along with the results of Monte Carlo simulations for the five known quarks, and, as an example, for a $35 \text{ GeV}/c^2$ top quark. The data agree well with the five-quark Monte Carlo, and only one event has an isolated track. The lower limits on masses of top and b' quarks decaying through virtual W bosons can be read off Fig. 23, which shows the expected number of events for these particles as a function of their masses.

Heavy neutral leptons will decay by mixing with light neutrinos, in analogy to the mixing which occurs among quarks. However, the mixing angles are completely

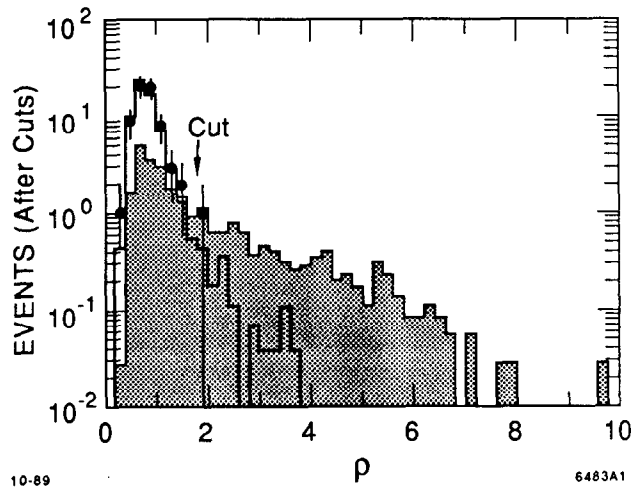


Fig. 22. The maximum isolation parameter ρ in each event. The solid line represents the result of a Monte Carlo simulation using the five known quarks. The shaded area shows the additional events that would be expected for a $35 \text{ GeV}/c^2$ top quark.

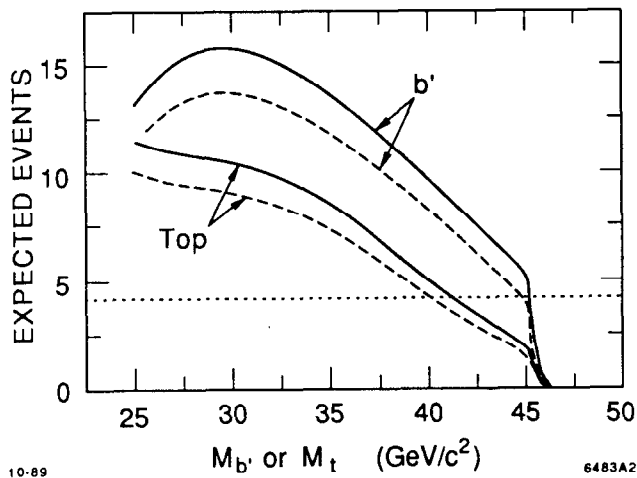


Fig. 23. The expected number of top and b' quark events (in which the quarks decay through virtual W 's) with at least one isolated track are shown by the solid lines. The dashed curves indicate the central value minus the uncertainty from statistical and systematic errors. The dotted line represents the upper bound at 95% C.L. for one observed event with background subtracted.

unknown and could be quite small. We thus display results as a function of the mixing matrix element squared, $|U_{L^0\ell}|^2$. Figure 24 shows the results of the isolated track search proper.

For very small values of $\sum |U_{L^0\ell}|^2$, the lepton will live long enough to fail our normal vertex requirements. We have explicitly searched for such decays by searching for events with vertices away from the interaction point.³² Figures 25 and 26 show the additional regions excluded, along with the results from previous experiments at lower energy.³³⁻³⁷ In general, smaller values of $|U_{L^0\ell}|^2$ than excluded in Figs. 25 and 26, will be excluded by limits on Γ_{inv} .

A search for isolated photons, which are defined to be photons with $\rho > 3.0$, found no events and set a limit of $m_{b'} > 45.4 \text{ GeV}/c^2$ at 95% C.L. for $B(b' \rightarrow b\gamma) \geq 25\%$.

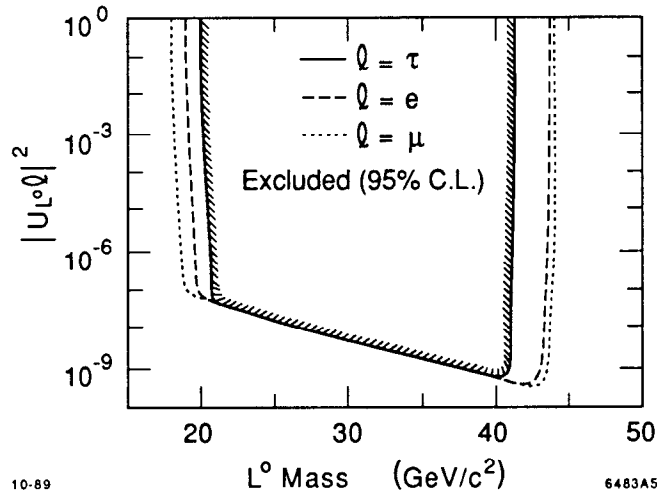


Fig. 24. Mass limits at the 95% C.L. for an unstable heavy neutral lepton L^0 as a function of mass and mixing matrix element squared for cases in which only one matrix element is important.

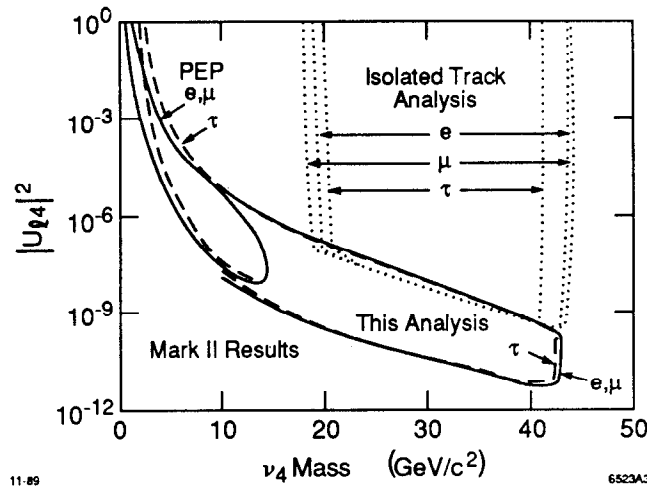


Fig. 25. Mass limits at the 95% C.L. for an unstable heavy neutral lepton ν_4 as a function of mass and mixing matrix element squared for cases in which only one matrix element is important. Also shown are the data from Fig. 24 and a MARK II search for detached vertices at PEP (Ref. 33).

The second type of search is for nonplanar events. Since three jets must lie in a plane, this, in effect, is a search for events with four or more jets. This is sensitive to new particle production since heavy new particles will decay into two or three jets. Since they are produced in pairs, they will yield events with four to six jets.

The variable which is used for this search is m_{out} defined as

$$m_{out} \equiv \frac{E_{cm}}{E_{vis}} \frac{1}{c} \sum |p_{out}| \quad , \quad (17)$$

where p_{out} is the momentum component out of the event plane as determined by the sphericity tensor, and the sum is taken over all charged and neutral particles. A non-planar event is defined to be one with $m_{out} > 18$ GeV.

Figure 27 shows the distribution of m_{out} for the data along with the Monte Carlo simulation predictions for the five known quarks, and, as an example, a $35 \text{ GeV}/c^2$ b' quark decaying into a charged Higgs boson and a c quark.

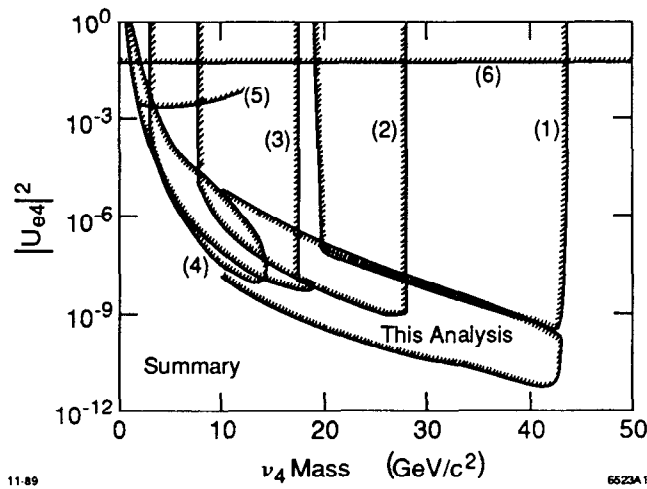


Fig. 26. Mass limits at the 95% C.L. for an unstable heavy neutral lepton ν_4 as a function of mass and mixing matrix element squared $|U_{L^0 e}|^2$. Also shown are the data from (1) Fig. 24, (2) AMY (Ref. 35), (3) CELLO (Ref. 36), (4) MARK II at PEP (Ref. 33), (5) monojet searches at PEP (Ref. 37), and (6) universality (Ref. 34).

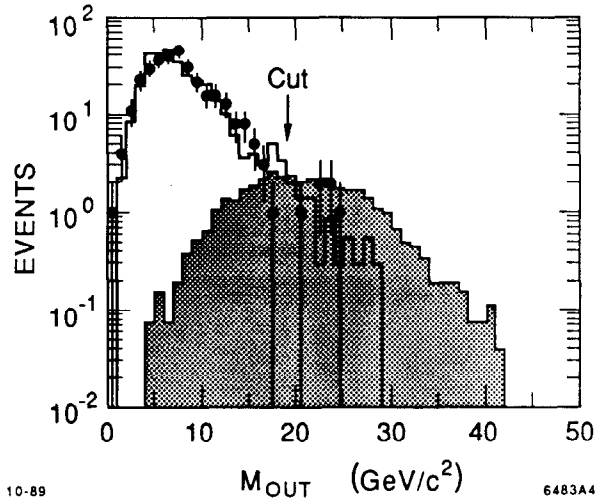


Fig. 27. The distribution of M_{out} . The solid line represents the result of a Monte Carlo simulation using the five known quarks. The shaded area shows the additional events that would be expected for a $35 \text{ GeV}/c^2$ b quark decaying into a charged Higgs boson and a c quark.

Six nonplanar events are found in the data, compared to five to twelve events expected from different Monte Carlo models of the known process. All of the limits are summarized in Table 3. The lower limits on the masses of new quarks and neutral leptons range from $40 \text{ GeV}/c^2$ to the kinematic limit of around $45 \text{ GeV}/c^2$.

New quarks that decay through virtual W 's are ruled out by experiments at hadron colliders up to a mass of $77 \text{ GeV}/c^2$.^{38,39} The new aspect of the limits in Table 3 are the ones which rule out all hadronic decay modes, which are difficult to detect with hadron colliders.

Although these limits are evaluated explicitly for the cases of new quarks and leptons, the techniques are fairly general and indicate that there is no new heavy particle production at the level of about 3% of the Z cross section.

Table 3. Summary of mass limits.

Particle	Decay Products (B.R. 100%)	Topology	Mass Limit (95% C.L.) (GeV/c ²)
top	bW^*	isolated track	40.0
	bW^*	m_{out}	40.7
	bH^+	m_{out}	42.5
b'	cW^*	isolated track	44.7
	cW^*	m_{out}	44.2
	cH^-	m_{out}	45.2
	$b + \text{gluon}$	m_{out}	42.7
	$b\gamma$, B.R. $\geq 25\%$	isolated photon	45.4
L^0	eW^*	isolated track	43.7
	μW^*	isolated track	44.0
	τW^*	isolated track	41.3

SUMMARY

The major physics results from the MARK II are:

- a precise measurement of the Z mass, $m = 91.14 \pm 0.12 \text{ GeV}/c^2$,
- a measurement of the number of light neutrino species, $N_\nu = 2.8 \pm 0.6$, which corresponds to $N_\nu < 3.9$ at 95% C.L.,
- a study of the partonic structure of hadronic decays, which shows good agreement with the expectations from QCD,
- a measurement of the strong coupling constant, $\alpha_s = 0.123 \pm 0.009 \pm 0.005$ at 91 GeV, and
- a search for new quarks and leptons which sets lower limits on their masses in the range 40 to 45 GeV/c².

REFERENCES

1. B. Richter, *Nucl. Instrum. Meth.* **136**:47 (1976).
2. The nine MARK II institutions are: California Institute of Technology, University of California at Santa Cruz, University of Colorado, University of Hawaii, Indiana University, Johns Hopkins University, Lawrence Berkeley Laboratory, University of Michigan, and Stanford Linear Accelerator Center. The present members of the collaboration are: G. S. Abrams, C. E. Adolphsen, R. Aleksan, J. P. Alexander, D. Averill, J. Ballam, B. C. Barish, T. Barklow, B. A. Barnett, J. Bartelt, S. Bethke, D. Blockus, W. de Boer, G. Bonvicini, A. Boyarski, B. Brabson, A. Breakstone, F. Bulos, P. R. Burchat, D. L. Burke, R. J. Cence, J. Chapman, M. Chmeissani, D. Cords, D. P. Coupal, P. Dauncey, H. C. DeStaebler, D. E. Dorfan, J. M. Dorfan, D. C. Drewer, R. Elia, G. J. Feldman, D. Fernandes, R. C. Field, W. T. Ford, C. Fordham, R. Frey, D. Fujino, K. K. Gan, C. Gatto, E. Gero, G. Gidal, T. Glanzman, G. Goldhaber, J. J. Gomez Cadenas, G. Gratta, G. Grindhammer, P. Grosse-Wiesmann, G. Hanson, R. Harr, B. Harral, F. A. Harris, C. M. Hawkes, K. Hayes, C. Hearty, C. A. Heusch, M. D. Hildreth, T. Himel, D. A. Hinshaw, S. J. Hong,

- D. Hutchinson, J. Hylen, W. R. Innes, R. G. Jacobsen, J. A. Jaros, C. K. Jung, J. A. Kadyk, J. Kent, M. King, S. R. Klein, D. S. Koetke, S. Komamiya, W. Koska, L. A. Kowalski, W. Kozanecki, J. F. Kral, M. Kuhlen, L. Labarga, A. J. Lankford, R. R. Larsen, F. Le Diberder, M. E. Levi, A. M. Litke, X. C. Lou, V. Lüth, G. R. Lynch, J. A. McKenna, J. A. J. Matthews, T. Mattison, B. D. Milliken, K. C. Moffeit, C. T. Munger, W. N. Murray, J. Nash, H. Ogren, K. F. O'Shaughnessy, S. I. Parker, C. Peck, M. L. Perl, F. Perrier, M. Petradza, R. Pitthan, F. C. Porter, P. Rankin, K. Riles, F. R. Rouse, D. R. Rust, H. F. W. Sadrozinski, M. W. Schaad, B. A. Schumm, A. Seiden, J. G. Smith, A. Snyder, E. Soderstrom, D. P. Stoker, R. Stroynowski, M. Swartz, R. Thun, G. H. Trilling, R. Van Kooten, P. Voruganti, S. R. Wagner, S. Watson, P. Weber, A. Weigend, A. J. Weinstein, A. J. Weir, E. Wicklund, M. Woods, G. Wormser, D. Y. Wu, M. Yurko, C. Zaccardelli, and C. von Zanthier.
3. G. S. Abrams *et al.*, *Nucl. Instrum. Meth.* **A281**:55 (1989).
 4. G. G. Hanson, *Nucl. Instrum. Meth.* **A252**:343 (1986).
 5. G. S. Abrams *et al.*, *IEEE Trans. Nucl. Sci.* **NS-25**:309 (1978) and **NS-27**:59 (1980).
 6. G. S. Abrams *et al.*, *Phys. Rev. Lett.* **63**:2173 (1989).
 7. J. Kent *et al.*, SLAC-PUB-4922 (1989); M. Levi, J. Nash, and S. Watson, SLAC-PUB-4654 (1989); and M. Levi *et al.*, SLAC-PUB-4921 (1989).
 8. F. A. Berends, R. Kleiss, and W. Hollik, *Nucl. Phys.* **B304**:712 (1988); S. Jadach and B. F. L. Ward, University of Tennessee report UTHEP-88-11-01 (1988).
 9. R. N. Cahn, *Phys. Rev.* **D36**:2666 (1987), Eqs. (4.4) and (3.1).
 10. J. Alexander *et al.*, *Phys. Rev.* **D37**:56 (1988).
 11. Calculated using the program EXPOSTAR, assuming $m_t = m_H = 100 \text{ GeV}/c^2$. D. C. Kennedy *et al.*, *Nucl. Phys.* **B321**:83 (1989).
 12. A. Sirlin, *Phys. Rev.* **D22**:2695 (1980).
 13. G. S. Abrams *et al.*, *Phys. Rev. Lett.* **63**:1558 (1989).
 14. T. Sjöstrand, *Comput. Phys. Commun.* **39**:347 (1986); T. Sjöstrand and M. Bengtsson, *Comput. Phys. Commun.* **43**:367 (1987); M. Bengtsson and T. Sjöstrand, *Nucl. Phys.* **B289**:810 (1987).
 15. G. Marchesini and B. R. Webber, *Nucl. Phys.* **B238**:1 (1984); B. R. Webber, *Nucl. Phys.* **B238**:492 (1984).
 16. T. D. Gottschalk and D. Morris, *Nucl. Phys.* **B288**:729 (1987).
 17. T. D. Gottschalk and M. P. Shatz, *Phys. Lett.* **150B**:451 (1985); Caltech reports CALT-68-1172, -1173, -1199 (1985).
 18. W. Bartel *et al.*, *Z. Phys.* **C43**:325 (1986).
 19. A. Petersen *et al.*, *Phys. Rev.* **D37**:1 (1988); S. Bethke *et al.*, *Z. Phys.* **C43**:325 (1989).
 20. C. Berger *et al.*, *Z. Phys.* **C12**:297 (1982).
 21. M. Althoff *et al.*, *Z. Phys.* **C22**:307 (1984).
 22. D. Bender *et al.*, *Phys. Rev.* **D31**:31 (1985).
 23. S. Bethke *et al.*, *Phys. Lett.* **B213**:235 (1988).

24. W. Braunschweig *et al.*, *Z. Phys.* **C41**:359 (1988); W. Braunschweig *et al.*, *Phys. Lett.* **B214**:286 (1988).
25. I. H. Park *et al.*, *Phys. Rev. Lett.* **62**:1713 (1989).
26. H. J. Behrend *et al.*, DESY Preprint 89-019 (1989).
27. Y. K. Li *et al.*, KEK Preprint 89-34 (1989); Y. K. Li, S. Olsen (private communication).
28. S. Komamiya *et al.*, SLAC-PUB-5137 (1989).
29. G. Kramer and B. Lampe, *Fortschr. Phys.* **37**:161 (1989)
30. G. S. Abrams *et al.*, *Phys. Rev. Lett.* **63**:2447 (1989).
31. V. Barger *et al.*, *Phys. Rev.* **D30**:947 (1984); *Phys. Rev. Lett.* **57**:1518 (1986); W. Hou and R. G. Stuart, *Phys. Rev. Lett.* **62**:617 (1989).
32. C. K. Jung *et al.*, SLAC-PUB-5136 (1989).
33. C. Wendt *et al.*, *Phys. Rev. Lett.* **58**:1810 (1987).
34. M. Gronau, C. N. Leung, and J. L. Rosner, *Phys. Rev.* **D29**:2359 (1984); V. Barger, W. Y. Keung, and R. J. Phillips, *Phys. Lett.* **B141**:126 (1984).
35. N. M. Shaw *et al.*, *Phys. Rev. Lett.* **63**:1342 (1989).
36. H.-J. Behrend *et al.*, *Z. Phys.* **C41**:7 (1988).
37. F. J. Gilman and S. H. Rhie, *Phys. Rev.* **D32**:324 (1985).
38. C. Albajar *et al.*, *Z. Phys.* **C37**:505 (1988).
39. F. Abe *et al.*, University of Pennsylvania Report UPR-0172E.